On the Oxidation of the Third-Generation Single-Crystal Superalloy CMSX-10

A. AKHTAR, M.S. HOOK, and R.C. REED

The oxidation behavior of the third-generation nickel-base single-crystal superalloy CMSX-10 is examined. Since the in-service performance of the alloy is of the greatest practical significance, a detailed study is made of the microstructural degradation of a turbine blade that had been removed prematurely from a commercial gas turbine engine. The results are augmented with isothermal oxidation tests conducted in the laboratory for 100 hours, at temperatures of 800 °C, 900 °C, and 1000 °C. Scanning electron microscopy (SEM), energy-dispersive X-ray (EDX) analysis, microhardness testing, and X-ray diffraction (XRD) were employed. It was found that the oxidation of CMSX-10 at temperatures below 1000 °C does not produce either Al_2O_3 or the spinel $Ni(Cr,Al)_2O_4$, both of which are found in the internal oxidation zone of the earlier generations of superalloys. Surprisingly, it is demonstrated conclusively that the oxidation of CMSX-10 generates the β phase (NiAl). This reaction, which to the authors' knowledge has not yet been reported, is termed self-aluminization. The XRD studies demonstrate that the internal oxidation of CMSX-10 produces $(Ni,Co)Ta_2O_6$, $(Ni,Co)WO_4$, $CrTaO_4$, and $Cr(W,Mo)O_4$. There is indication that the formation of the δ phase (Ni_2Al_3) slows the oxidation rate at 1000 °C.

I. INTRODUCTION

THE turbine blading required for a modern gas turbine engine is now very often cast in single-crystal form, to avoid the grain boundaries that re deleterious to the creep and fatigue properties. There continues to be significant evolution in the compositions of the alloys designed for these applications, with the latest ones containing significant quantities of the transition metals, rhenium and ruthenium, which markedly improve the mechanical properties. However, the operating temperatures of the gas stream continue to rise such that the degradation of the blading during service, by oxidation or corrosion, is a strong possibility, as will be demonstrated in this article. For this reason, it is usual to protect the blading using coating technology, *e.g.*, either by aluminization or by the application of a ceramic thermal barrier layer with a metallic bond coat.

Unfortunately, for various reasons, it is not always possible to apply coatings to the superalloys. Therefore, the mechanisms of oxidation and corrosion are of the greatest importance, not only for the coating, but also for the bare superalloys themselves; consequently, much work continues to be reported on this topic. For example, the oxidation characteristics have been examined in recent years for the aluminized[1–7] and uncoated[1,2,3,7–12] second-generation single-crystal superalloys. However, the third-generation superalloy, CMSX*-10, contains refractory metals (W + Mo + Re + Ta) at a total content of 19.4 wt pct and a Cr concentration of 2.0 wt pct, as compared with 16.1 and 6.5 wt pct, respectively, for its second-generation counterpart, CMSX-4.[13] In common with other third-generation superalloys such as RENÉ* N6, the low chromium content of CMSX-10 raises concerns about whether the resistance to oxidation will be adequate in the environment under which the blade is to operate.[7] Of note here is the oxidation of the third-generation superalloy RENÈ N6. That alloy, which has a (W + Mo + Re + Ta) content of 19.7 wt pct, a value similar to that of CMSX-10 but with a higher Cr content of 4.5 wt pct, was oxidized in the laboratory at 1200 °C.[14] It was found that reducing the sulfur content to a level below 0.1 ppm prevented spalling of the scale, which results from thermal cycling. In another recent investigation, the Re content was varied in Ni-8Cr-2Ti-10Al-Re and Ni-8Cr-2Ti-15Al-Re alloys[15] (the concentrations expressed in atomic percent), and it was found that alloys with a Re/Al ratio of 0.1 exhibited only a small mass change, which resulted from oxidation. This observation led to the suggestion that the Re/Al ratio is a good indicator of the resistance to oxidation.

Clearly, at this stage, there is a need for detailed microstructural studies, in order to reveal the underlying mechanisms of degradation, so that this physical understanding can be accounted for as the alloy compositions become refined further. A further point is that there is always a difference between the isothermal oxidation behavior studied in the laboratory and the cyclic response relevant to engine conditions. In this article, a detailed microstructural characterization is carried out on a third-generation, single-crystal superalloy, CMSX-10. A turbine blade that had been removed from service after a number of flight cycles was examined. This provided a unique insight into the behavior of this material under the conditions most relevant to the design intent. The investigation was augmented with isothermal oxidation carried out in the laboratory.

*CMSX is a trademark of Cannon-Muskegon Co., Muskegon, MI.

*RENÉ is a trademark of General Electric Co., Fairfield, CT.

A. AKHTAR, Adjunct Professor, is with the Department of Materials Engineering, The University of British Columbia, Vancouver, BC, Canada, V6t 1Z4. Contact e-mail: akhtar@cmpe.ubc.ca M.S. HOOK, formerly Graduate Student, Department of Materials Science and Metallurgy, University of Cambridge, Cambridge, CB2 3QZ, United Kingdom, is Investment Banker, Deutsche Asset Management, 1 Appold Street, London EC2A 2UU, UK. R.C. REED, Professor, is with Department of Materials, Imperial College, London, South Kensington Campus, London SW7 2AZ, United Kingdom.

Manuscript submitted July 13, 2004.

Tests were conducted on coupons heated to 800 °C, 900 °C, and 1000 °C for 100 hours.

II. EXPERIMENTAL DETAILS

The turbine blade considered in this study (Figure 1(a)) was approximately 150 mm long. It had been in service in a commercial aero-engine for 12633 flight hours, experiencing 3266 takeoffs and landings. To reduce the centrifugal stresses experienced during service, the blade contained a single large cavity, which ran from the shroud to the root, and was thus hollow. However, this intermediate-pressure (IP) blade was not designed to receive cooling air. It should be noted that the external surface of the blade had undergone pack-aluminization treatment, to protect it from oxidation and corrosion during operation. Hence, only very minimal oxidation had occurred on the outer surface. However, the internal surface of the hollow blade had not received the aluminization treatment and thus had been degraded quite significantly. In the present study, it is the oxidation of this bare interior surface that is studied in detail. In Table I is given the nominal composition of the CMSX-10 superalloy from which the turbine blade was cast in single-crystal form, with the <001> direction nearly parallel to the axis of the blade. Concentrations of Re (2.0) and Al (13.2) yield a Re/Al ratio of 0.15, a value in excess of the critical maximum of 0.1 quoted recently for good oxidation resistance.[15] As noted earlier, the Cr content of 2.0 wt pct (2.4 at. pct) in the CMSX-10 is lower than the typical value of 6.5 (7.5) found in CMSX-4. Significant quantities of Co (3.2), Ta (2.8), W (1.7), and Mo (0.3) are also present. All the figures in parentheses are in atomic percent.

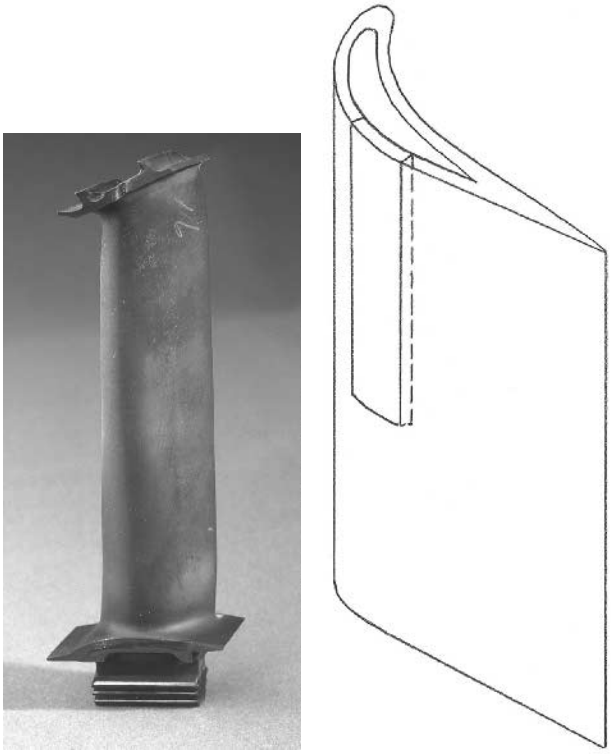

(*a*) (*b*)

Fig. 1—(*a*) A photograph of the blade investigated in the present work. (*b*) A schematic drawing showing the orientation of the coupon used in the XRD study.

Table I. Nominal Composition of CMSX-10

	Al	Co	Cr	Hf	Mo	Ni	Re	Ta	Ti	W
At. pct	13.2	3.2	2.4	<0.1	0.3	bal	2.0	2.8	0.2	1.7
Wt pct	5.7	3.0	2.0	0.03	0.4	bal	6.0	8.0	0.2	5.0

To facilitate detailed examination, specimens were cut from the blade, using electrodischarge machining (EDM). Two types of specimens were used. Transverse sections approximately 2 mm thick were taken from three regions: the midsection of the blade, close to the root, and near the shroud. These sections were mounted and prepared for metallographic examination using scanning electron microscopy (SEM). Elemental analysis was carried out using the energy-dispersive X-ray (EDX) attachment to the SEM, at an accelerating voltage of 20 kV, on polished but unetched transverse sections. The estimated accuracy for the elements O, Al, Ti, Cr, Co, and Ni is within 2 at. pct of the indicated concentration, and within 5 pct for Mo, Hf, Ta, W, and Re.

For the X-ray diffraction (XRD) analysis, a longitudinal specimen was used, as shown schematically in Figure 1(b). This was taken from the trailing face of the blade close to the leading edge, and between the shroud and the midsection. It had a length of approximately 40 mm, measured along the blade axis; therefore, there was little, if any, curvature in this dimension. However, there existed a slight curvature along the 12-mm width of the specimen. The concave side of the specimen contained the oxidation-associated microstructure of the CMSX-10 under consideration, and this surface was the focus of the XRD work. The absence of curvature along the length of this specimen enabled the narrow but approximately 10-mm-long beam of X-rays from the diffractometer slit to be incident upon essentially a flat surface of the specimen. This enabled the 2θ values to be determined accurately, in spite of the slight curvature of the specimen in the transverse direction. A diffractometer was used in the work employing Cu K_α radiation, to generate the diffraction patterns. The scanning rate was 0.5 deg/min. The phases present were identified using the JCPDS-ICDD database (International Centre for Diffraction Data, Newton Square, PA).

The disc specimens used for the isothermal tests were developed by making transverse cuts on a 10-mm-diameter single-crystal rod that had its axis at less than 8 deg from a <100> direction. The single-crystal rod, which was grown using the same composition, directional solidification apparatus, and settings as used for the blade for the commercial casting of the single-crystal blades, was heat treated in a manner identical to that employed for the blade. Isothermal oxidation tests were carried out in the laboratory using a chest furnace under static air for up to 100 hours at 800 °C, 900 °C, and 1000 °C. The temperature range for the isothermal tests was selected to cover adequately the range the IP blade was expected to encounter in service. Samples polished to a 1-μ diamond finish were positioned in an alumina crucible and placed in the furnace. Care was taken not to examine the face that remained in contact with the crucible. Oxidation kinetics trials were performed on a purpose-built thermal gravimetric

analysis (TGA) apparatus comprising of a digital recording microbalance and a vertical tube furnace. Discs, 10 mm in diameter and 1.6 mm thick, were suspended from the balance into the furnace by means of a platinum wire and a platinum sample holder. The faces of the discs were polished to a metallographic finish. The change in the initial mass of approximately 1 g was measured with an accuracy of 1 μg. Any mass loss attributed to the formation and subsequent evaporation of PtO_2 was accounted for through the subtraction of the background.

The Laue back-reflection method was employed for determining the orientation of the single-crystal blade. The X-ray beam was directed at right angles to a transverse section of the blade. For microhardness testing, the diamond pyramid indenter was used with a load of 50 g.

III. RESULTS

The axis of the blade, from an analysis of the Laue back-reflection diffraction pattern, was found to be inclined to a <100> direction at 9 deg, thus making the transverse sections of the blade nearly parallel to a (001)-type plane.

A. *The SEM Analysis*

Microstructural features, as observed on the transverse section from near the shroud, are shown in Figures 2(a) through (c). Note that the hollow portion of the blade appears dark. The trailing edge lies to the left of the micrograph, whereas the leading and the trailing faces are located above and below it, respectively. The following observations may be made from Figure 2(a). First, oxidation has resulted in the formation of two distinct domains: a scale on the exposed surface and an oxidation reaction domain (ORD) extending into the metal. Second, the interface between these two domains is cracked, except at the extreme left of the micrograph. The scale thickness varied from a minimum of less than 20 to a maximum of around 130 μm on this section. Discontinuities in the ORD are seen in the lower portion of the figure. Furthermore, the scale thickness correlates with

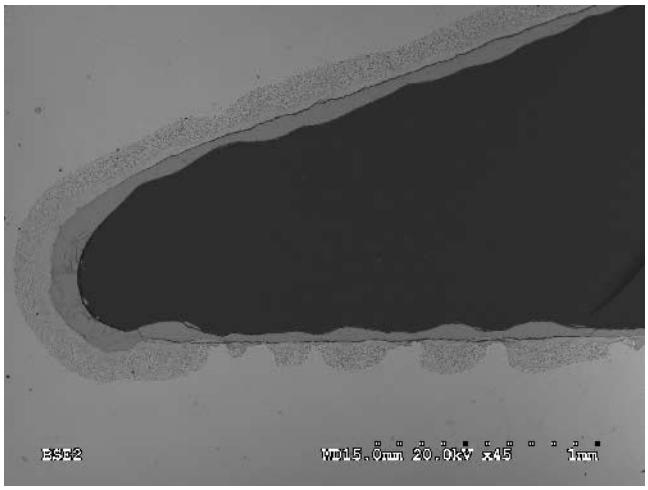

(*a*)

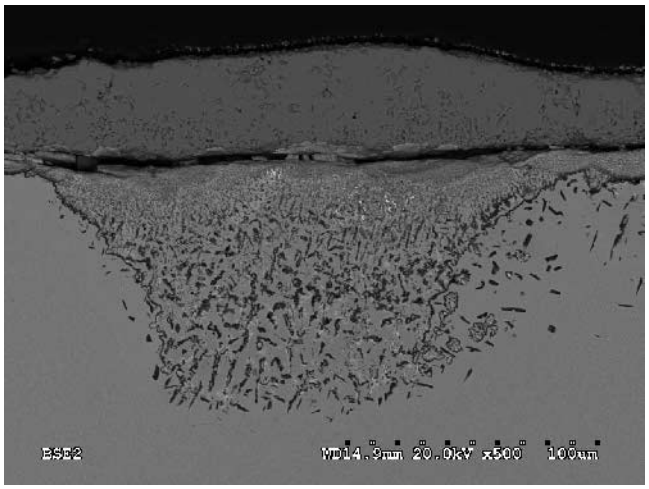

(*b*)

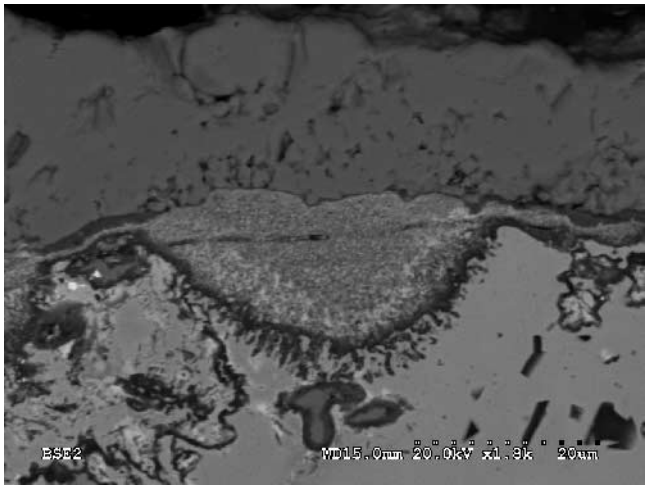

(*c*)

Fig. 2—Scanning electron micrographs from a transverse section near the shroud: (*a*) an overview of the microstructure adjacent to the cavity in the blade; (*b*) a higher-magnification image of one of the isolated oxidation reaction domains seen below the blade cavity in (a); and (*c*) details of a small, isolated oxidation reaction domain.

the thickness of the ORD: the thicker the scale, the thicker the ORD.

Figure 2(b) shows the details of the microstructure associated with one of the discontinuous ORDs of Figure 2(a), at a higher magnification. It is clear that the cracking occurred not at the interface between the scale and the ORD, but within the ORD close to the scale. Furthermore, what appeared to be a single discontinuous ORD under a low magnification (Figure 2(a)) is, in fact, a result of the coalescence of at least three ORDs lying adjacent to one another (Figure 2(b)). A fine microstructure appears in the regions where these ORDs nucleated, with a coarser microstructure seen at a greater depth.

Figure 2(c) shows the details associated with a small ORD that had not yet coalesced with any other. Clearly, the interface between the 22-μm-thick scale and the small-discontinuous ORD lying below it is intact. The microstructure associated with the ORD as seen in the figure may be broadly divided into two distinct zones. One is a nearly semielliptical fine-structure zone (FSZ). Debonding is seen in the upper portion of the FSZ. The transition zone (TZ) lies below the FSZ, and extends to the base material. It should be noted that backscattered electrons (BSE) were used for the imaging of the SEM photographs shown in Figure 2. Therefore, the darker regions represent either the enrichment with elements that have low atomic numbers or the depletion of elements that have high atomic numbers, or a combination thereof. Conversely, the lighter regions signify either the depletion of elements that have low atomic numbers or the enrichment of elements that have high atomic numbers, or a combination thereof.

The TZ in Figure 2(c), which appears to be separated from the FSZ by a thin dark layer, contains a variety of dispersed phases within it. Adjacent to the FSZ are needles emanating from the thin dark layer, below which lie irregular globules and distinct geometric shapes. Each geometric shape has a dark core surrounded by a gray boundary, which separates it from the surrounding matrix.

Figure 3(a) shows the oxidation-induced microstructure observed near the leading edge of the section taken from the middle portion of the blade. Significant portions of the scale became detached from the blade. The remaining scale is thick (140 μm), as is the associated ORD (210 μm), thus making the total thickness of the oxidation-induced microstructure 350 μm. The ORD was found to be continuous across the entire midsection of the blade. In other words, the discontinuous ORDs found on the section near the shroud (Figure 2(a)) were absent in the midsection of the blade. A noteworthy feature of the continuous ORD shown in Figure 3(a) is that the entire TZ appears to be made up of a needle- or a plate-shaped phase dispersed in a gray matrix. Although the dispersed phase had four distinct orientations, one of the four remained preferred for the growth of the needles. Preferential growth occurred in the orientation that was closest to being perpendicular to the exposed surface.

The interface region between the continuous ORD (Figure 3(a)) and the parent material is shown in greater detail in Figure 3(b). The microstructure of the CMSX-10 parent material consists of submicron-sized cuboids of γ' separated by thin layers of γ, as expected. The dispersed geometric shapes are seen adjacent to the base material. It is clear that the edges of these geometric shapes remain parallel to either the sides or the diagonals of the cuboids.

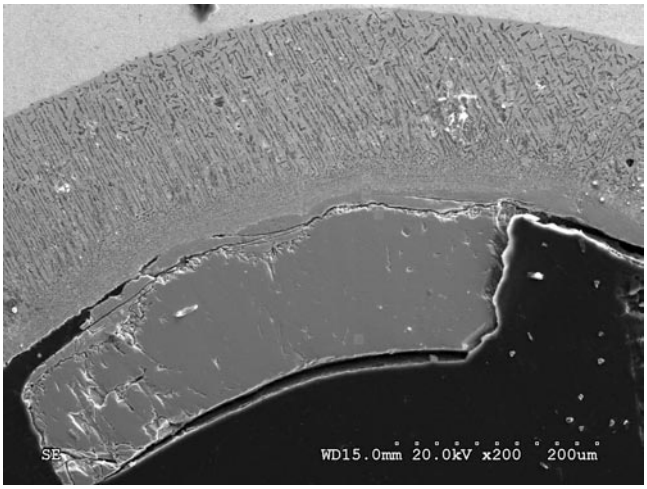

(*a*)

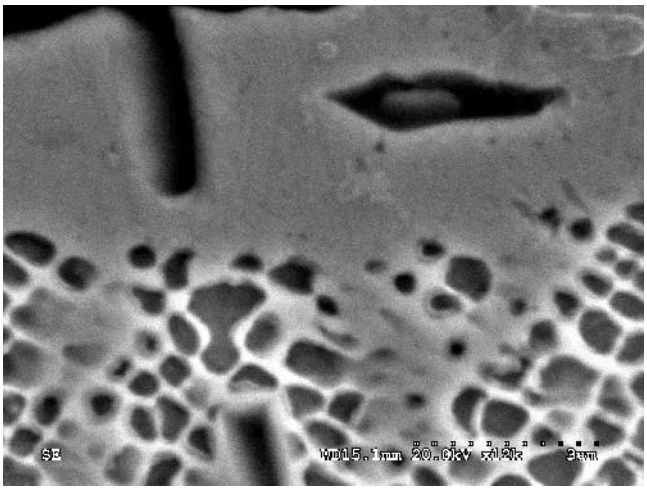

(*b*)

Fig. 3—Scanning electron micrographs from the midsection near the leading edge: (*a*) a remnant of the external scale and a continuous ORD and (*b*) the interface region between the base material and the continuous ORD.

B. *The EDX Analysis*

The element-concentration-*vs*-depth plots are shown in Figures 4 and 5, for the regions containing the continuous ORD (Figure 3(a)) and the small-discontinuous ORD (Figure 2(c)), respectively. Small areas were analyzed as opposed to using the point scanning mode. This was done with the objective of establishing the overall concentration of each element at a given depth, rather than of analyzing each microconstituent present in the structure. The window sizes used were 15 $\times$ 15 μm, for the continuous ORD (Figure 4), and 2.5 $\times$ 2.5 μm, for the small-discontinuous ORD (Figure 5). Three vertical lines are shown on each figure. They demarcate the boundaries between the distinct regions identified. The line on the left is the interdomain boundary between the scale and the ORD; the one on the right distinguishes the ORD from the base material. The transition from the FSZ to the TZ, both within the ORD, is indicated by the line in the middle. The following observations may be made from Figures 4 and 5.

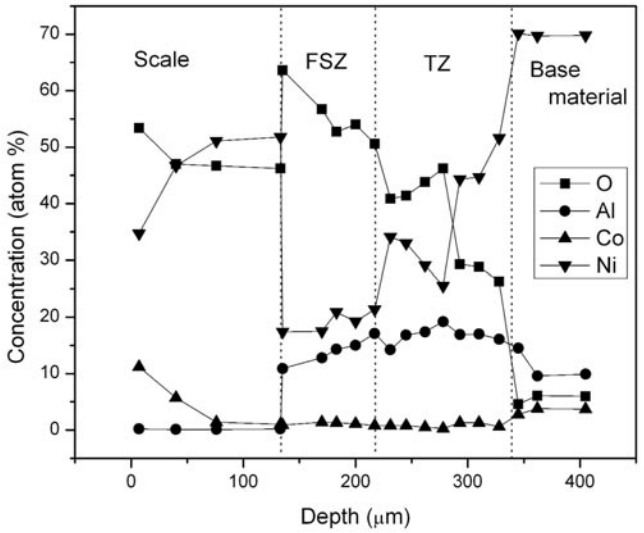

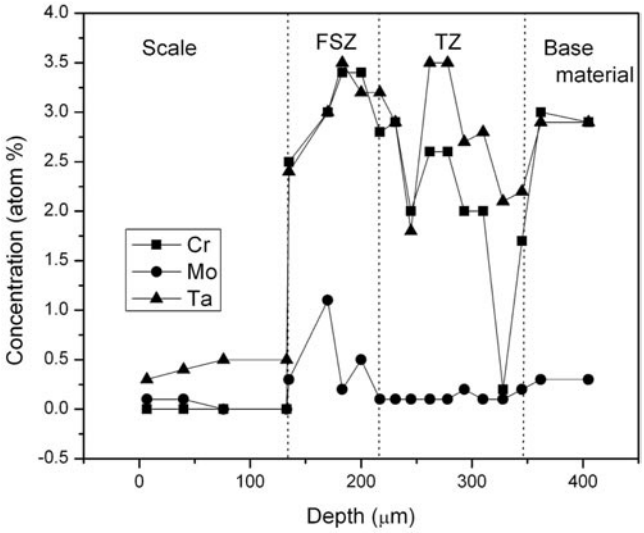

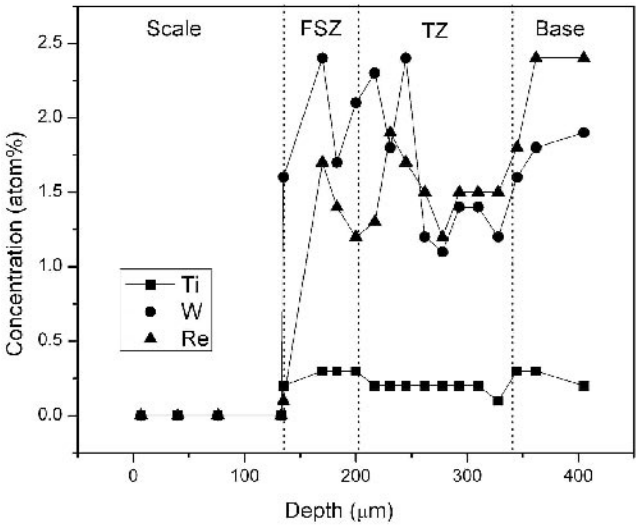

Fig. 4—Element concentration from EDX analysis *vs* depth for the continuous ORD and the adjacent regions shown in Fig. 3(a).

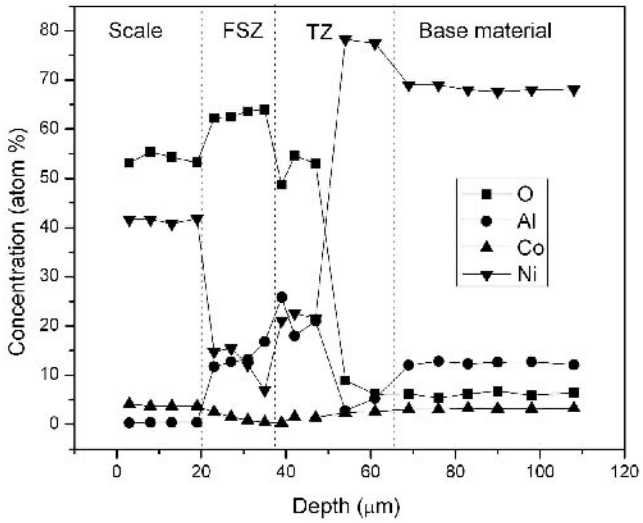

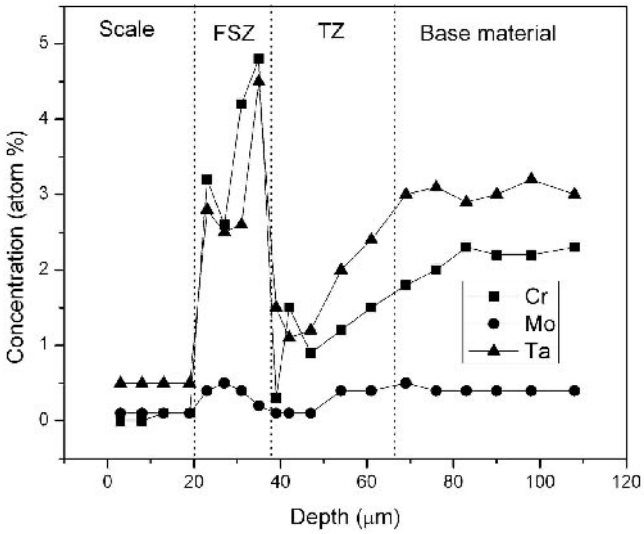

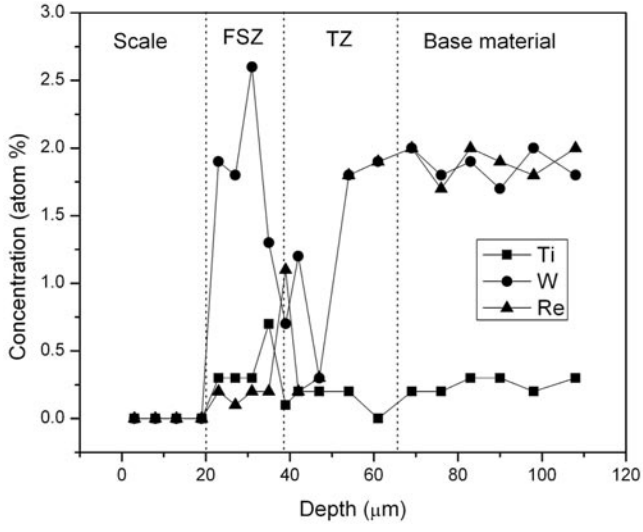

Fig. 5—Element concentration from EDX analysis *vs* depth for the small-discontinuous ORD in Fig. 2(c) and the adjacent regions.

First, the scale contains predominantly O, Ni, and Co. All the other elements analyzed were present only in negligible proportions, with the exception of a small amount (<0.5 pct) of Ta. The concentration of Co was found to be at a maximum near the exposed surface of the scale. The cumulative concentration of Ni and Co was approximately

equal to the concentration of oxygen in the scale, indicating that the scale is of the type (Ni,Co)O.

Second, abrupt changes occurred in the concentrations of virtually all the elements at the interface between the scale and the ORD. The concentrations of Al and all the refractory elements (Cr, Ta, W, Mo and Re) increased. There was also an increase in the concentration of oxygen. In fact, the highest concentration of O was found in the FSZ. However, the concentrations of Ni and Co decreased. The change in the Ni concentration was most dramatic. Even though this element was present on either side of the interface, its concentration dropped from more than 48 pct in the scale to less than 16 pct in the FSZ of the continuous ORD (Figure 4). The corresponding drop in the case of the small-discontinuous ORD (Figure 5) was from 42 to 15 pct. At greater depths, the Ni content increased, in general. The lowest concentration of Ni was found to lie both here and elsewhere inside the FSZ. Below the scale, the concentration of Al increased with depth, in general, attaining a maximum in the TZ. Although a subsequent decrease occurred in the concentration of Al with depth, the nature of the variation differed, depending on the type of ORD examined. In the continuous ORD, the Al concentration decreased with depth, monotonically, to its level in the base material. By contrast, the lowest concentration of Al occurred for the small-discontinuous ORD in the region adjacent to the base material.

Finally, at depths below the scale, the concentrations of all the refractory elements increased. The highest concentrations of Cr, Mo, Ta, W, and Re were found inside the FSZ. The lowest concentrations of these elements were found in the TZ. Titanium also attained its peak concentration in the FSZ. The Hf (not shown in Figures 4 and 5, for clarity) attained its highest concentration in the TZ. The lowest concentrations of the latter two elements were found in the ORD (Figure 5), the same region in which the lowest concentrations of the other refractory elements were found. In the small-discontinuous ORD (Figure 5), the lowest values of Ti and Hf were found at depths different from those at which the lowest values were found for Cr, Mo, Ta, W, and Re.

A further point of note is that the highest concentrations of all the refractory elements reached inside either type of ORD were higher than their corresponding values in the base material. This was true of Cr, Mo, Ta, W, Ti, and Hf. However, Re was an exception in this regard. The concentration of Re was found to be higher in the base material than anywhere inside the ORD. A probable explanation for the lower concentration of Re near the surface is the evaporation loss of its oxide, since the latter is known to be volatile at the temperatures to which the blade was exposed in service.

C. *The XRD Analysis*

On the internal surfaces of the blade, the scale was lost in places, but elsewhere it remained attached only loosely, so that it proved possible to strip the scale from the surface. The underside of the scale could be distinguished readily from the exposed top surface: the underside had an olive green color, whereas the top surface was gray.

The XRD patterns were taken from the stripped scale (Figure 6) and from the coupon stripped of the scale (Figure 7). Figures 6(a) and (b) show the diffraction patterns from the top and the bottom (underside) surfaces of the scale. The intensity of the reflected X-ray beam is plotted against 2θ, where θ is the angle of incidence. It is seen from Figure 6(b) that all the major peaks expected from the cubic lattice of NiO are present. Although a similar pattern was obtained from the top face (Figure 6(a)), the observed peaks are shifted to slightly lower 2θ values than those expected for pure NiO. For example, reflections from (111) and (311) of pure NiO are to be expected at the 2θ values of 37.3 and 75.4 deg, respectively; however, the measured values were 37.1 and 75.1 deg. These shifts to lower 2θ values (associated higher lattice spacing or d values) are consistent with the higher cobalt content of the

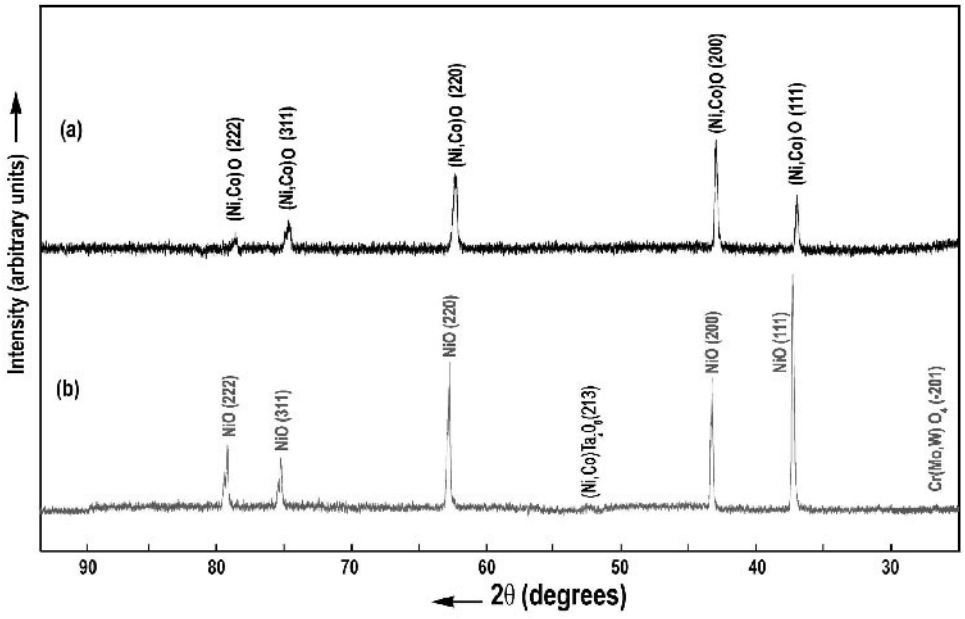

Fig. 6—The XRD patterns of the scale removed from the blade: (*a*) the top face (exposed while attached) and (*b*) the bottom face.

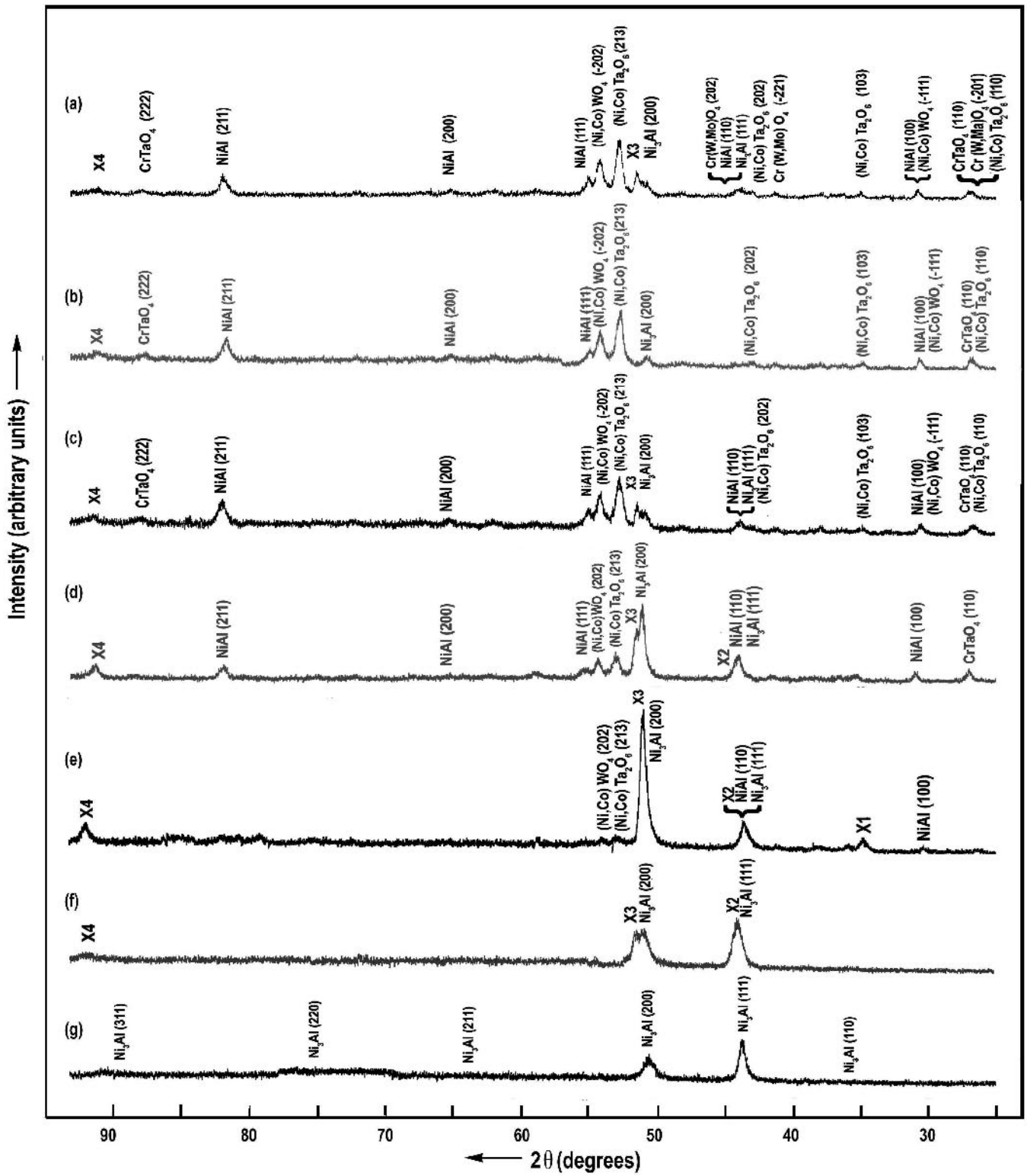

Fig. 7—The XRD patterns obtained from the coupon after the following treatments in succession: (*a*) stripping of the scale, (*b*) immersion in Aqua Regia for 20 min, and (*c*) through (*g*) successive abrasion steps.

top face than that of the bottom face (Figure 4). A further point to note is that, in the diffraction pattern from the bottom face of the scale (Figure 6(b)), there are two minor reflections in addition to those coming from the NiO lattice. These two peaks are labeled as reflections from the (−2 0 1) planes of the monoclinic lattice of $Cr(Mo,W)O_4$ and from the (2 1 3) planes of the tetragonal lattice of $(Ni,Co)Ta_2O_6$. The identification of these two peaks is based on the assumption that the underside of the stripped scale had contaminants that were present in larger quantities on the stripped surface of the blade coupon.

Additional reflections from these two lattices were present in the diffraction pattern from the scale-stripped surface of the coupon, as seen in Figure 7(a). The identities of the standard patterns found applicable in indexing the diffraction peaks obtained in the present work are listed in Table II. Reflections that could not be identified through available standard patterns are designated X1, X2, X3, and X4, in Figure 7. Those four peaks are a result of reflections from the (110), (111), (200), and (311) planes, respectively, of the alloy-depleted CMSX-10 base material, as suggested by the following consideration.

First, the peaks X1, X2, X3, and X4 occurred at only slightly higher 2θ values than those expected from the base metal reflections (110), (111), (200), and (311), respectively. For example, X3 was found to be at 51.2 deg, as compared with the base metal reflection (200), which was at 50.7 deg. Similarly, X2 was located at 44 deg, as compared with 43.6 deg for the (111) reflection from the base material (Figure 7(f)). Although the single-crystal orientation remained such that the (110) and (311) reflections from the base metal were not recorded in the present work (Figure 7(g)), the peaks X1 and X4 were also present at slightly higher values than the expected locations of those two reflections, respectively, from the base material. Assuming that the peaks X1 to X4 came from the depleted zone, the change in the lattice parameter of the depleted zone with respect to that of the base material may be computed from the positions of these and the corresponding base metal reflections. Since the base metal reflections were not recorded from the (110) and (311) planes (Figure 7(g)), the calculations were restricted to the (200) and (111) reflections only, the latter having produced peaks from the base material and the depleted zone (Figure 7(f)). This procedure resulted in the change in lattice parameter Δa, as calculated from the X-ray data of $(-29 \pm 3) \times 10^{-4}$ nm.

This change in lattice parameter calculated from the X-ray data may be compared with that computed using the compositions of the depleted zone and the base material, the latter two having been measured in the present work employing EDX (Figures 4 and 5), and the known values of the change in lattice parameter[16,17,18] of the binary solid solutions of Ni (γ phase) as well as that due to ternary additions into Ni_3Al (γ' phase). Of note here is that the compositions are not the same for the depleted zone associated with the continuous ORD (Figure 4) and that due to the small-discontinuous ORD (Figure 5). Therefore, two sets of calculations were made, one for each type of ORD. For the continuous ORD, it was found that the change in the lattice parameter of the depleted zone with respect to the base material would be -6×10^{-4} nm, whether the depleted zone had a γ structure or a γ' structure. In the case of the small-discontinuous ORD, however, the Δa value was found to be -28×10^{-4} nm for a γ-phase structure of the depleted zone, and -6×10^{-4} nm, when the structure of the depleted zone is γ'. It will be demonstrated later in this article that the composition of the depleted zone associated with the small-discontinuous ORD does, in fact, belong in the γ-phase field (Figure 11(b)). Thus, it would appear that the figure of $(-29 \pm 3) \times 10^{-4}$ nm, computed from the XRD data for the change in the lattice parameter of the depleted zone with respect to the base material, is in excellent agreement with the -28×10^{-4} nm calculated from the EDX data of the small-discontinuous ORD. Although this independent corroboration of the change in the lattice parameter gives credence to the assumption that the reflections X1, X2, X3, and X4 are attributable to the depleted zone, the process also raises the question as to why the reflections from the depleted zone of the small-discontinuous ORD, and not those from the continuous ORD, have been recorded in the XRD pattern (Figure 7). There are two possible explanations for this. First, the X-ray coupon was taken from near the trailing face of the blade (Figure 1), which remains cooler than the leading face. Since the ORDs found in the cooler regions of the blade are discontinuous (Figure 2(a)), it is likely that the coupon contains many discontinuous ORDs. Second, the change in lattice parameter of the depleted zone from that of the base material is small (-6×10^{-4}), which may result in line broadening rather than in a distinct peak shift. A peak shift may be resolvable with XRD equipment that has better resolution than does the apparatus used in the present work.

Table II. Standard Patterns Found Applicable for the Indexing of Diffraction Patterns in the Present Work

Material	JCPDS-ICDD	Structure and Lattice Parameters (Å)
CoO	9–402	cubic; $a = 4.260$
$CoNiO_2$	10–188	cubic; $a = 4.240$
NiO	4–835	cubic; $a = 4.177$
Ni_3Al	9–97	cubic; $a = 3.572$
NiAl	2–1261	cubic; $a = 2.880$
NiAl (Ni-rich)	20–19	cubic; $a = 2.887$
$NiTa_2O_6$	32–702	tetragonal; $a = 4.718$, $c = 9.170$
$CoTa_2O_6$	32–314	tetragonal; $a = 4.738$, $c = 9.170$
$CrTaO_6$	39–1428	tetragonal; $a = 4.642$, $c = 3.020$
$NiWO_4$	15–755	monoclinic; $a = 4.600$, $b = 5.665$, $c = 4.912$
$CoWO_4$	15–867	monoclinic; $a = 4.948$, $b = 5.683$, $c = 4.669$
$CrWO_4$	34–197	monoclinic; $a = 9.271$, $b = 5.828$, $c = 4.644$
$CyMoO_4$	34–474	monoclinic; $a = 9.240$, $b = 5.815$, $c = 4.629$

Figure 7 shows a series of diffraction patterns obtained from the X-ray coupon removed from the blade (Figure 1(b)), following the stripping of the scale noted earlier. Removal of the scale enabled the X-rays to penetrate into the material located under it. Prior to this stripping, the coupon produced a diffraction pattern characteristic only of the top surface of the scale (Figure 6(a)), suggesting that the penetration was not sufficient enough to reach the bottom portion of the scale, which produces a different diffraction pattern (Figure 6(b)). The coupon was given a series of treatments, each in succession, before being washed in ethanol and dried and placed back in the same position on the diffractometer specimen holder. Figure 7(a) shows the diffraction pattern after the stripping of the scale. Immersion in Aqua Regia (3 parts HCl, one part HNO_3) for 20 minutes followed next, and the diffraction pattern that resulted is shown in Figure 7(b). The purpose of the Aqua Regia treatment was to identify a constituent or constituents that might have been at the exposed surface and that could be dissolved away by the acid treatment. Abrasion with 320-grit emery

paper followed. Abrasion was interrupted five times. These abrasion steps were intended to achieve an end similar to that of the stripping of the external scale, *i.e.*, to enable the X-rays to penetrate deeper into the material in succession, thus providing information on the structures of the microconstituents that could not be had without this series of abrasions. Although the geometry of the blade coupon did not permit the quantification of the layer thickness removed in each step, the abrasion steps followed with XRD did provide valuable insight, as seen in Figures 7(c) through (g). Further abrasion of the coupon surface did not change the diffraction pattern. Thus, it is inferred that Figure 7(g) represents the diffraction pattern of the base material. It is seen from Figure 7(g) that the CMSX-10 single crystal remained oriented such as to produce only the (111) and the (200) reflections on the diffraction pattern. The positions of the other reflections to be expected from a powder specimen in place of the single crystal are also indicated on the diffraction pattern, for information only. The other reflections were not found in the single-crystal pattern recorded in the present work. Moreover, it is noteworthy at this juncture that the lattice parameters of the γ and the γ' phases are rather similar in CMSX-10, so that all reflections from the disordered γ phase would coincide with some of the reflections from the ordered γ' phase (Ni_3Al structure).

The reflections in Figure 7(a) are interpreted as follows. The major reflections are from the oxides $(Ni,Co)Ta_2O_6$ and $(Ni,Co)WO_4$. The two other oxides were identified as $CrTaO_4$ and $Cr(W,Mo)O_4$. However, surprisingly, aluminum oxide Al_2O_3, which is usually formed upon oxidation of the uncoated second-generation superalloys,[1–3,7,9–12] was completely absent in the oxidation-induced microstructure of the CMSX-10 examined in the present work. The two anticipated reflections from the base material (Figure 7(g)) are seen in Figure 7(a). These two are labeled Ni_3Al (111) and Ni_3Al (200), although, as noted earlier, these also correspond to the same reflections from the disordered γ phase. Moreover, five reflections were identified as coming from the β phase (the analog of the intermetallic compound NiAl in the binary phase diagram). They are labeled NiAl (100), NiAl (110), NiAl (111), NiAl (200), and NiAl (211), with the strongest reflections coming from the (111) and the (211) planes (Figures 7(a) through (d)). These two reflections are distinct. A third NiAl peak from (200), although small, is also distinct. The two remaining are overlapped with reflections from the base material and an oxide. In the former category is NiAl (110), which is overlapped with Ni_3Al (111) and $Cr(W,Mo)O_4$ (202). The latter, NiAl (100), is overlapped with $(Ni,Co)WO_4(-111)$. Last, the reflections X3 and X4 are from the (200) and (311) planes of the alloy-depleted lattice, as indicated earlier.

Some noteworthy effects of the Aqua Regia treatment, as seen from a comparison of Figures 7(a) and (b), are the elimination of both the (200) reflection from the alloy-depleted material (X3) and the reflections associated with the oxide $Cr(W,Mo)O_4$. However, the $CrTaO_4$ peaks remained unaffected. Figure 7(c) shows the diffraction pattern upon the initial abrasion with emery paper following the Aqua Regia treatment. The reemergence of the (200) reflection from the alloy-depleted material (X3) is the most prominent effect. The results of the next stage of abrasion are seen in Figure 7(d). The intensities of the reflections from the oxides have decreased, as a result. However, the reflections from the base material and those from the alloy-depleted material (X3 and X4) are stronger. Moreover, a broadening of the superimposed NiAl (110)/Ni_3Al (111) peak toward a higher 2θ value suggests the presence of the (111) reflection from the alloy-depleted material (X2).

Figure 7(e) shows the results of further abrasion. Reflections from the oxides and from the intermetallic compound NiAl have all but vanished. The (200) reflection from the alloy-depleted material (X3) has grown enormously, so as to swamp the adjoining (200) reflection from the base material. Moreover, the reflection (311) from the alloy-depleted material (X4) is clearly established, as is the (110) reflection from the alloy-depleted material (X1).

Yet more abrasion produced the diffraction pattern seen in Figure 7(f). At this point, there are no traces left of the reflections from either the oxides or the intermetallic β phase. The reflections from the alloy-depleted material have become less intense. For example, the intensities of the (200) reflections from the alloy-depleted material and the base material are comparable. Finally, as seen from Figure 7(g), the only reflections present are those from the CMSX-10 base material.

D. *Isothermal Oxidation*

Figure 8 shows the change in the mass of the disc specimens with time, for up to 100 hours during isothermal tests conducted at 800 °C, 900 °C, and 1000 °C. At 800 °C, the mass gain occurs at a rapid rate initially, but this rate of increase becomes smaller at longer exposures. However, there continues to be a mass gain with time even at 100 hours. A similar trend is observed at 900 °C, with the difference that, for any given exposure time, the mass gain remains higher at the higher temperature. This trend continues into the early stage of exposure at 1000 °C, *i.e.*, the mass gain at 1000 °C remains higher than the mass gains at the lower temperatures of 900 °C and 800 °C, for up to about 16 hours. However, there occurs little mass change

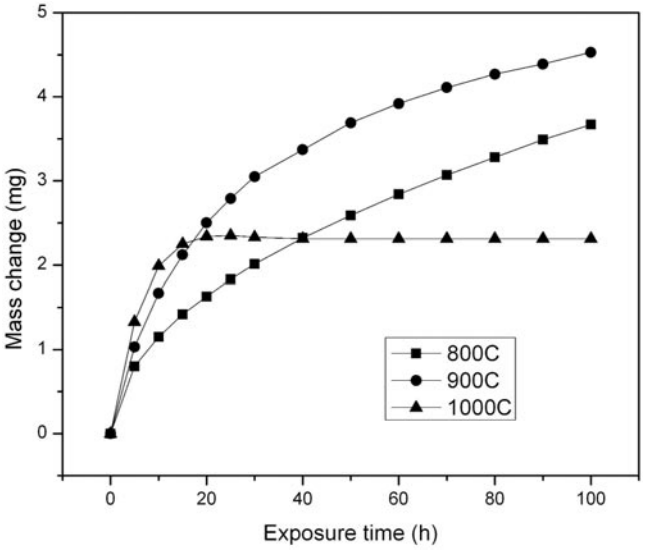

Fig. 8—Mass change with time for isothermal exposures at 800 °C, 900 °C, and 1000 °C.

for exposure times in excess of around 20 hours at 1000 °C. In fact, at exposure times beyond 20 hours, there occurs a slight mass loss, up to around 40 hours. Thereafter, the mass of the specimen remains unchanged with time for exposure times up to 100 hours, at which point the test was terminated.

Figure 9 shows the transverse sections of the discs after the isothermal tests were completed in the laboratory. The scale and the ORD seen on the surface of the blade removed from service (Figures 2 and 3) are also observed with the discs having undergone the isothermal tests. It is seen from Figure 9(a) that, at the lowest test temperature of 800 °C, the scale is thin (10 μm) but detached from the disc. At the intermediate temperature of 900 °C (Figure 9(b)), the scale is thicker, but also detached from the substrate. A scale with an intermediate thickness, but well bonded to the disc, is seen on the specimen that underwent the isothermal test at 1000 °C. Moreover, the ORD also has a maximum thickness at the intermediate temperature (900 °C). Furthermore, the spikes associated with the continuous ORD observed on the blade removed from service (Figure 3(a)) are seen in the specimen tested isothermally at 900 °C.

E. *Microhardness vs Depth Profiles*

Figure 10 shows the diamond pyramid hardness (DPH) profiles generated from the cross-sections of the blade and the isothermally treated coupons. Two regions of the blade were examined: one at the midsection located close to the hottest region, the other close to the root that experienced a lower temperature exposure in service. The isothermally treated coupons had been exposed for 100 hours at 900 °C and 1000 °C, respectively. As seen from the figure, both the base material of the coupons and the blade sections had hardness in the vicinity of 375 DPH.

In the blade midsection, the hardness increased in the TZ containing the spikes, to attain a maximum of around 650 DPH; however, a peak hardness of 1300 DPH was obtained in the FSZ adjacent to the external NiO scale. The external scale (NiO) had a hardness of around 300 DPH; the

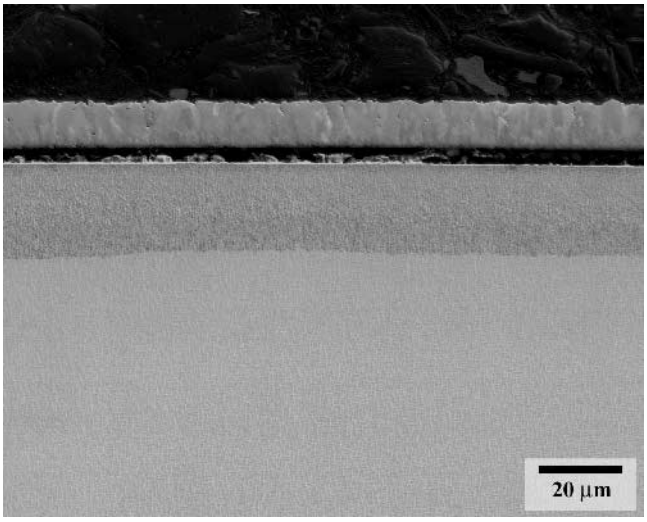

(*a*)

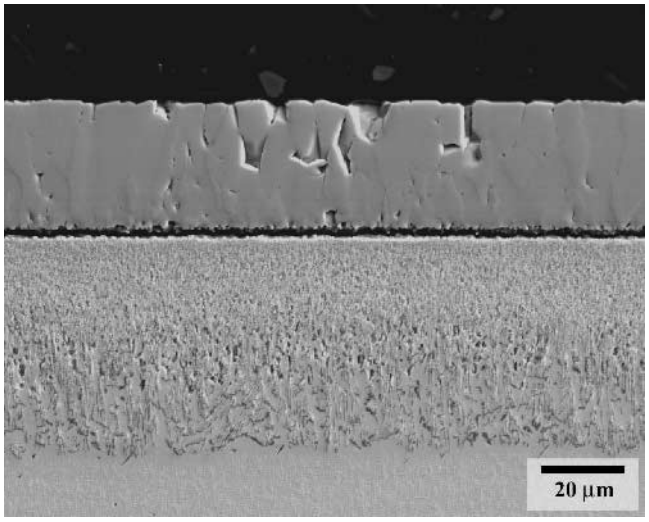

(*b*)

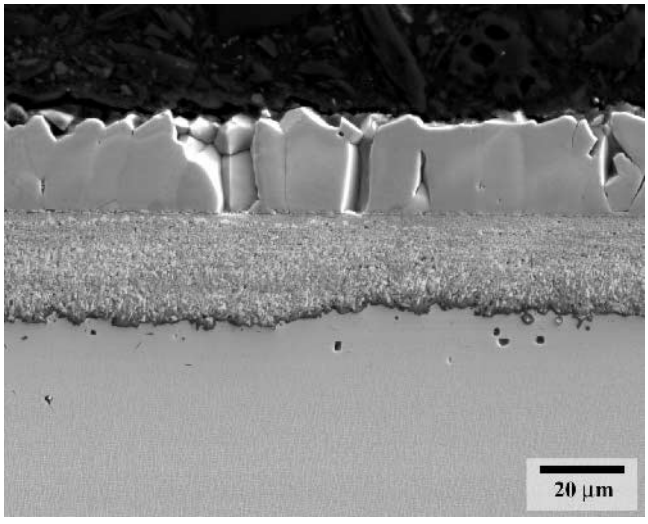

(*c*)

Fig. 9—Transverse sections of discs after 100 h of exposures to (*a*) 800 °C, (*b*) 900 °C, and (*c*) 1000 °C.

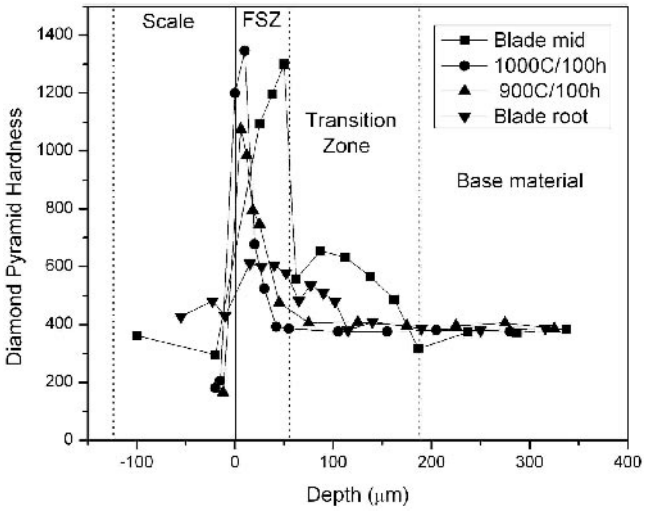

Fig. 10—Microhardness *vs* depth profiles. Note that, for clarity, only the positions of the interfaces as observed on the blade midsection are shown as vertical dotted lines.

value remained slightly higher closer to the exposed portion of the scale, possibly due to the strengthening caused by the presence of a concentration of cobalt that was higher there than at the scale near the FSZ (Figure 4). A similar trend is observed at the blade root region, although the lower temperature exposure of this region of the blade has produced a lower peak hardness of only 520 DPH, as compared with 1300 DPH in the corresponding region of the midsection of the blade that had experienced a higher temperature exposure. Although the short exposure of 100 hours had produced a relatively thin scale and a narrow ORD, as compared with those found on the blade, the effect of temperature was similar. A harder FSZ, which had a DPH of 1350, was found with the higher isothermal treatment temperature of 1000 °C; this was harder than the FSZ of 1080 DPH that was found for the specimen exposed isothermally at 900 °C.

IV. DISCUSSION

An external NiO scale forms upon oxidation in the laboratory in a variety of Ni-base superalloys having a ($\gamma + \gamma'$) microstructure.[3,7,9,10,12,19–21] Moreover, experiments conducted on the first- and second-generation cast single-crystal superalloys PWA* 1480, PWA 1484, and CMSX-4 have shown that an external scale of α-Al_2O_3 is created following a transition period during which NiO is formed.[3] Therefore, the observation of an external NiO scale on the turbine blade made of CMSX-10 is not altogether surprising in the present work. However, it is clear from the present work that Al_2O_3 is not formed, in spite of the turbine blade having undergone a prolonged exposure in excess of 12000 hours and involving over 3000 cycles. A further point of note is that no evidence has been found in the present work for the formation of the spinel $Ni(Al,Cr)_2O_4$ on the oxidized turbine blade of the third-generation superalloy CMSX-10. In some of the earlier generations of the superalloys, the spinel has been found at the α-Al_2O_3/gas interface.[9,22,23] More significant, however, is the finding in the present work that the β phase is generated as a result of the oxidation of CMSX-10 (Figure 7). To the best of the authors' knowledge, the formation of the β phase resulting from the oxidation of the bare surface of a Ni-base superalloy has not been reported earlier. Since this observation sets the oxidation behavior of CMSX-10 apart from that of the earlier generations of superalloys, the process of nucleation and growth of the β phase, and its role in the internal oxidation of the superalloy, are now discussed further.

*PWA is a trademark of the Pratt and Whitney Co., East Hartford, CT.

A. *Generation of the* β *Phase during the Oxidation of CMSX-10*

In a binary Ni-Al alloy, the stoichiometric γ' phase may be represented as 75Ni25Al and the stoichiometric β phase as 50Ni50Al. In principle, therefore, a transformation into β is possible when Ni is removed from or Al is added to γ'. From Figures 4 and 5, it is seen that Ni depletion has occurred adjacent to the scale. Clearly, this is a result of the removal of Ni to the surface to form the external NiO scale.

Is this depletion sufficient to have formed the β phase that is clearly evident in the XRD patterns (Figure 7)? Quantitatively, the transformation to the stoichiometric β phase requires a depletion of 25 at. pct Ni from γ', since the binary phase diagram shows[24] that the latter is stable only in a narrow composition range of just over 1 pct at 900 °C, the estimated average operating temperature of the turbine blade examined in the present work. However, the β phase remains stable at as high as 62 at. pct Ni at that temperature. Therefore, the nucleation of the β phase from γ' could begin as soon as the Ni content drops down to around 73 at. pct; the complete transformation of γ' into β would have occurred when the Ni content dropped down to a value below 62 at. pct in the binary alloy. The EDX data generated in the present work (Figures 4 and 5) show that the base material has a Ni content of around 70 at. pct, and that the Ni concentration just below the scale has values of 17 and 15 pct, respectively, for the continuous and the small-discontinuous ORDs. The latter concentrations of Ni are well below those that would have caused a complete transformation of the ($\gamma + \gamma'$) base material into β in the region just below the scale, had the material been a binary Ni/Al alloy. However, CMSX-10 contains at least nine alloying elements of significance (Table I). Therefore, the impact of elements other than Ni and Al must be taken into account in considering the transformation of γ' into β in CMSX-10.

It is known[35] that Co occupies the *a*-sites, which are normally filled by the Ni atoms of the γ' lattice; on the other hand, Ti, Mo, Ta, W, and Hf, occupy the *b*-sites, which are normally filled by an Al atom. However, Cr, may fill either of the positions. The position occupied by Re is at present unknown. Based on the knowledge that Pd and Pt occupy the a-sites,[35] however, an assumption will be made here that Re occupies the *a*-sites. Thus, a parameter Σ Ni may be defined, which is the sum of the concentrations of Ni and the Ni-like elements (Co and Re) in CMSX-10. Similarly, Σ Al may be defined as the sum of the concentrations of Al and the Al-like elements (Ti, Mo, Ta, W, and Hf) in the superalloy. Plots of Σ Ni/(Σ Ni + Σ Al) *vs* depth are shown in Figure 11, using the concentration profiles of the continuous and the small-discontinuous ORD (Figures 4 and 5).

The simple concentration ratio Ni/(Ni + Al), *i.e.*, excluding elements that are Ni-like and Al-like, is also plotted in the figure, for comparison. Moreover, on the ordinate of Figure 11 are shown the positions of the phase boundaries of the binary Ni-Al phase diagram as they would be at 900 °C. Clearly, the simple concentration ratio Ni/(Ni + Al) is not a realistic indicator of the phases in equilibrium, because this parameter places the base material on the boundary between the γ and ($\gamma + \gamma'$) fields. The parameter Σ Ni/(Σ Ni + Σ Al), henceforth designated *C*, is a more realistic representation, since it places the base material well within the ($\gamma + \gamma'$) region, as it should be. As seen from Figure 11, *C* has values of 54 pct for the continuous ORD, and 51 pct for the small-discontinuous ORD, both just below the scale. These values place the composition well within the β-phase field, as is clear from Figure 11. It is noteworthy at this juncture that, should the assumption made regarding Re occupying the Ni sites be incorrect, with Re atoms occupying the Al sites instead, the values of *C* would be lower than those indicated in Figure 11, thus placing the composition of the FSZ even more solidly within the β phase than shown in the figure. Thus, not only is there the direct evidence for the formation of the β phase from the XRD results (Figures 7(a) through (e)), but also the measured composition profiles provide implicit evidence in support of the formation of the β phase.

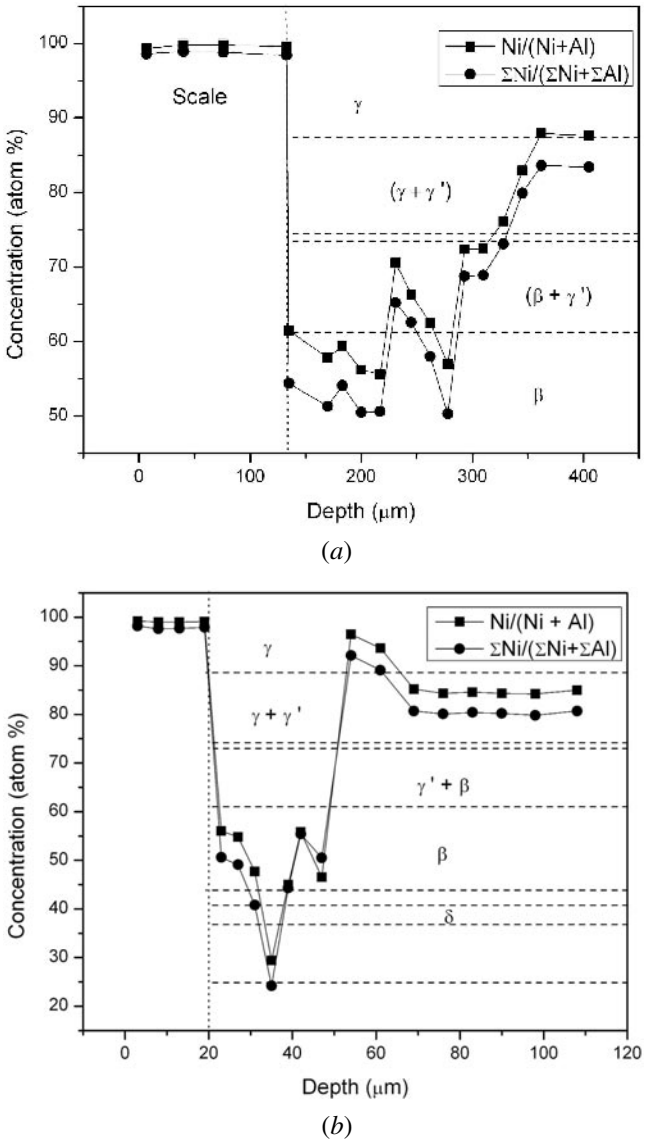

Fig. 11—Concentration ratios *vs* depth for the (*a*) continuous ORD and (*b*) small-discontinuous ORD.

Metallographic evidence for the presence of the β phase in the interface region between the scale and the ORD (Figures 2(b) and (c), and 3(a)) is obscured, due to the formation of the FSZ in that region. Even though the occurrence of internal oxidation has obliterated the metallographic evidence for it in this region, there exists β phase at the advancing oxidation front, as shown in Figure 12. On the top left of Figure 12 is the BSE image of the lower portion of the region shown in Figure 2(c). At the bottom of the BSE is seen the cuboid γ/γ' microstructure of the base material. The image at the bottom left of Figure 12 was made using the Al K_α secondary X-rays (aluminum map). The lighter regions have a higher concentration of Al than do the darker ones. Clearly, the dispersed geometric shapes are richer in Al. The image at the bottom right was constructed using the Ni $K_{\alpha 1}$ secondary X-rays. A lower concentration of Ni is indicated inside the dispersed geometric shapes, since they appear darker compared with their surroundings. Finally from the O K_α secondary X-ray image, shown on the top right, it is clear that the dispersed geometric shapes contain levels of oxygen similar to the surrounding material. In other words, the geometric shapes are not aluminum oxide, even though they are regions enriched in Al and depleted in Ni with respect to their surroundings. Clearly, the nucleation of the dark regions that have the geometric shapes has been brought about as a result of the Ni being removed from the nucleation site, and the Al diffusing into those regions from the surrounding regions. These observations point to the dark core as being the β phase, and to the dark gray boundary separating it from its surroundings as being the γ' phase (Figures 2(c), 3(b), and 12). The presence of the β phase, in the form of long spikes located ahead of the FSZ, is clearly seen with the continuous ORD (Figure 3(a)).

The crystallographic orientation relationships between the parent γ' phase and the transformed β phase, resulting from the oxidation of the superalloy CMSX-10, have not been examined in detail in the present work. However, the observation that the boundaries of the geometrically shaped β phase remain parallel to either the edges or the diagonals of the cuboids in the base material (Figures 3(b) and 12) suggests that the transformation into the β phase occurs on the (110) type planes of the γ' lattice, as might have been expected. Moreover, it is interesting to note that, under the conditions that led to the creation of the continuous ORD on the turbine blade (Figure 3(a)), the orientation relationship just described was maintained while the transformation progressed over distances on the order of 100 μm, thus giving rise to the four sets of plates seen in Figure 3(a).

B. *The Propagation of the* β *Phase and Internal Oxidation*

Clearly, the β phase is initiated below the scale (Figure 12), and it propagates into the depth of the material as the oxida-

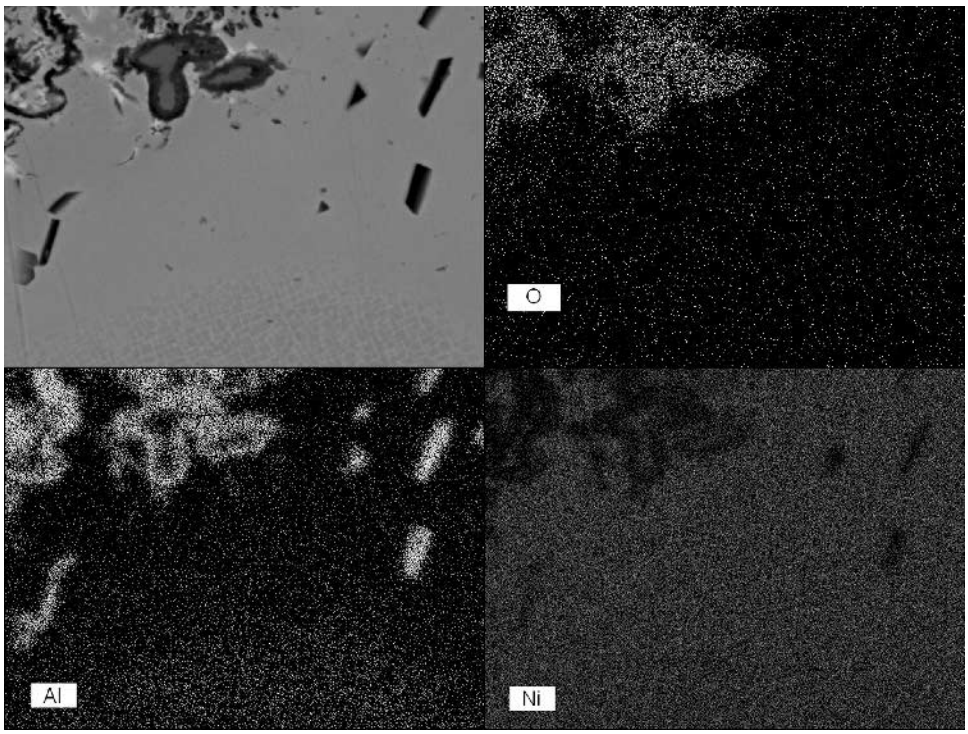

Fig. 12—The interface region between the small-discontinuous ORD (Figure 2(c)) and the base material, imaged using BSE imaging (top left), and the same region mapped using characteristic secondary X-rays from aluminum (bottom left), nickel (bottom right), and oxygen (top right).

Table III. Diffusion Coefficients (m^2/s) at 1273 K

Element	NiO	γ	γ'	β(62Ni)	β(52Ni)
Ni	4.2×10^{-16}[25]	3.7×10^{-16}[26]	8.3×10^{-17}[33]	8.0×10^{-14}[36]	4.0×10^{-16}[36]
Co		4.8×10^{-16}[27]	1.9×10^{-16}[34]		
Cr		7.1×10^{-16}[27]	1.0×10^{-17}[34]		
Al		2.0×10^{-15}[28]	7.1×10^{-17}[35]		
Ti		3.5×10^{-15}[29]	3.2×10^{-18}[34]		
Mo		3.8×10^{-16}[30]			
Hf		8.5×10^{-15}[31]			
Ta		1.5×10^{-15}[32]			
W		1.2×10^{-16}[32]			
Re		2.5×10^{-17}[32]			

tion of CMSX-10 progresses (Figures 3(a) and (b), 11, and 12). The discussion that follows will consider the mechanism involved in the propagation of the β phase, and its role in bringing about internal oxidation.

It is clear from Figure 2(a) that the oxidation of CMSX-10 begins with the formation of the external NiO scale containing some Co (Figures 4(a) and 6). Moreover, we have postulated in the earlier discussion that the resulting depletion of Ni from the region adjacent to the scale brings about formation of the β phase. This creation of the β phase at the scale/metal interface would aid the transfer of Ni to the scale, as seen from the diffusion data summarized in Table III. The Ni-rich β phase to form first in the process (for example, 62Ni38Al shown in the table), would permit the diffusion of Ni faster at 1000 °C by approximately three orders of magnitude than would be the case in γ' at that temperature. Should the composition approach stoichiometry, the diffusion rate of Ni in the β phase would still remain higher than that in γ'. For example, Ni diffuses five times faster in 52Ni48Al (listed in Table III) than it does in γ' at 1000 °C. Thus, the β phase would tend to propagate rapidly upon being created. Moreover, there may be a localized temperature rise due to the exothermic nature of the reaction, which leads to the formation of the β phase.[37,38] Should such a localized rise in temperature take place, it would further accelerate the growth of the β phase into the depth of the material. The presence of the β phase at a depth of approximately 200 μm from the scale/metal interface, in the case of the continuous ORD (Figure 3), is a likely result of the propagation of the β phase in the manner described earlier.

The oxidation of the binary γ'-phase Ni_3Al occurs by means of two material transport processes: inward oxygen diffusion and outward Ni diffusion.[39] At 800 °C, oxidation occurs predominantly by outward Ni diffusion to form NiO, although a lesser amount of inward oxygen diffusion also occurs. The EDX data generated in the present work (Figures 4 and 5) show that inward diffusion of oxygen has occurred on the turbine blade made of CMSX-10. The concentration of oxygen remains at a higher level in the FSZ than in the scale, and it

Table IV. Enthalpies of Decomposition[25]

Oxide	ΔH (kJ)
Al_2O_3	1115.2
Ta_2O_5	817.6
Cr_2O_3	752.4
WO_2	589.0
MoO_2	587.7
NiO	480.7
CoO	477.3
ReO_2	424.3

decreases through the TZ of the ORD, to attain a relatively low level in the base material. Clearly, internal oxidation takes place, which leads to the formation of the FSZ. However, none of the stable oxides of the major alloying elements (Al, Ta, Cr, W, Mo, and Re) has been detected in the XRD patterns (Figure 7). As seen from Table IV, the enthalpies of decomposition of these oxides are high. It is likely, therefore, that a localized temperature rise occurs as a result of the formation of these oxides, which in turn produces the complex oxides that have been identified in the present work through XRD (Figure 7). The following reactions may be involved in the creation of the observed oxides in the internal oxidation zone (the FSZ):

$$Cr_2O_3 + 2WO_2 + O = 2CrWO_4 \quad [1]$$

$$Cr_2O_3 + 2MoO_2 + O = 2CrMoO_4 \quad [2]$$

$$Cr_2O_3 + Ta_2O_5 = 2CrTaO_4 \quad [3]$$

$$Ta_2O_5 + Ni + O = NiTa_2O_6 \quad [4]$$

$$WO_2 + Ni + 2O = NiWO_4 \quad [5]$$

The oxides containing aluminum are conspicuous due to their absence on the oxidized blade of CMSX-10 examined in the present work. The simple oxide of aluminum, Al_2O_3, and the spinel $Ni(Cr,Al)_2O_4$ are frequently formed when Ni-base superalloys are oxidized. Alpha alumina forms in the region adjacent to the base material of the second generation of the Ni-base superalloys.[9] It is clear from the present work that the third-generation superalloy CMSX-10, on the other hand, forms the β phase in place of the Al_2O_3 adjacent to the base material (Figures 3 and 12).

The formation of the β phase alters the course of events leading to the formation of the internal oxidation zone of CMSX-10. In place of the spinel $Ni(Cr,Al)_2O_4$, CMSX-10 forms $(Ni,Co)Ta_2O_6$, $(Ni,Co)WO_4$, $CrTaO_4$, and $Cr(Mo,W)O_4$. The reason for this change in the mechanism of the formation of the internal oxidation zone is not entirely clear at present, and more work is required to elucidate it. Possibly, the low Cr content of CMSX-10 is a factor.

C. *Isothermal Oxidation in Relation to Oxidation in Service*

Similarities exist in the features generated through isothermal oxidation at 900 °C found both in the laboratory and on the blade removed from service. These similarities are apparent in the microstructure as well as in the profiles of hardness and composition generated in the present work, as will become clear from the discussion to follow.

The microstructure of the blade cross-section (Figure 3(a)) shows that an external NiO scale is formed; the associated ORD is made up of a narrow band of the FSZ and a wide TZ, the latter comprised of long spikes of the β phase. These features are also seen in the microstructure of the isothermal test conducted at 900 °C for 100 hours. However, it is apparent that the degree of oxidation was far greater on the blade than in the isothermal test (Figures 3(a) and 9(b)). This difference is a result of the longer service exposure of the blade (12000 hours involving 3000 cycles), compared to the short isothermal exposure (100 hours in the laboratory at 900 °C).

To gain insight into the differences in the mass gain with time observed in the isothermal tests (Figure 8), specimens treated at 900 °C and 1000 °C were subjected to XRD and EDX analysis in a manner similar to that employed for the examination of the blade in the present work. The XRD patterns obtained from the discs that were treated at 900 °C but that did not have their surfaces abraded contained reflections from the NiO as well as the (Ni,Co)O lattice, as has been observed with the scale removed from the blade (Figure 6). It may be noted, however, that only the (Ni,Co)O reflections were seen on the diffraction pattern obtained from the top surface of the scale removed from the blade (Figure 6(a)); reflections from NiO, however, were seen in the diffraction pattern obtained from the bottom face of the scale removed from the blade (Figure 6(b)). The presence of reflections from both these lattices in the pattern obtained from the unabraded specimen isothermally treated at 900 °C is that the scale on the isothermally treated specimen was thinner than it was on the scale removed from the blade (Figures 3(a) and 9(b)). The thinner scale on the isothermally treated specimen enabled both lattices to produce reflections simultaneously, even though they might have been located on opposite sides of the scale, as was the case with the scale removed from the blade. The diffraction patterns that followed the successive abrasion steps of the oxidized surface revealed the presence of the oxides $(Ni,Co)Ta_2O_6$, $(Ni,Co)WO_4$, *etc*., along with the β phase and an absence of Al_2O_3 and the spinel $Ni(Cr,Al)_2O_4$ similar to that noted earlier from the examination of the blade oxidized in service (Figure 7). Similar results were obtained with the coupon isothermally treated at 1000 °C, with additional peaks that are tentatively identified as reflections from the δ phase (Ni_3Al_2). The δ phase was found to be located close to the base material, because these peaks made their appearance only when the abrasion had reached the stage in which the peaks from the base material were beginning to show. Moreover, the peaks attributed to the δ phase disappeared with additional light abrasion, leaving only the base material reflections. This suggested the possible presence of only a thin layer of the δ phase adjacent to the base material. Reflections from the (102) and the (110) planes of the δ phase were recorded. However, it is to be remembered that the Al-rich β phase also produces the (110) reflection close to that at which the (110) reflection from the δ phase occurs. Therefore, the X-ray data may at best be treated as a tentative identification of the δ phase. Corroboration in support of the formation of the δ phase was obtained from the EDX data, as will be seen from the following.

The EDX data obtained from two discs isothermally treated to 100 hours are presented in Figure 13, as a plot of Σ Ni/(Σ Ni + Σ Al) *vs* depth. The dotted horizontal lines shown on the figure are the phase boundaries as they would be at 900 °C

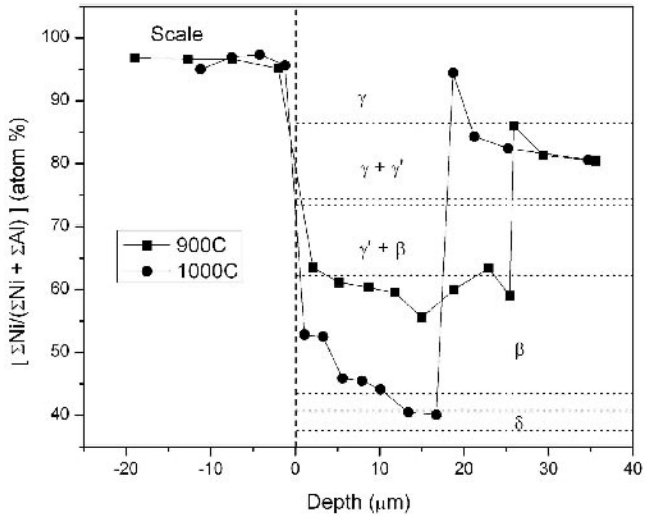

Fig. 13—The equivalent nickel content *vs* depth after isothermal exposures of 100 h each at 900 °C and 1000 °C.

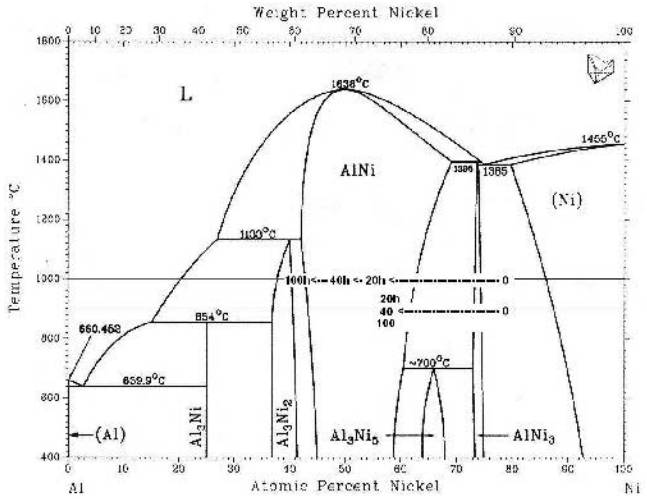

Fig. 14—A binary Ni-Al phase diagram shows the equivalent nickel content of the advancing oxidation reaction zone into the base material after 20, 40, and 100 h of isothermal treatments carried out at 900 °C and 1000 °C.

in the binary Ni/Al phase diagram, which is shown in Figure 14. It is seen from the binary phase diagram that the positions of the phase boundaries at Ni concentrations above 30 at. pct shift only slightly as a result of a change in temperature from 900 °C to 1000 °C. As a first approximation, therefore, the phase boundaries shown on Figure 13 may be treated as being valid for 900 °C as well as for 1000 °C. Two points of note emerge from Figure 13. First, there is similarity between the data obtained from the isothermal test conducted at 900 °C in the laboratory (Figure 13) and those obtained for the continuous ORD examined on the blade removed from service (Figure 11(a)). Second, the oxidation behavior is different at 1000 °C than it is at 900 °C. With reference to the first point, the Σ Ni/(Σ Ni + Σ Al) values at all depths remain close to the $\beta/(\beta + \gamma')$ phase boundary, and the composition of the alloy-depleted zone created at the interface between the advancing ORD and the base material remains within the $(\gamma + \gamma')$ phase field, *i.e.*, the composition of the alloy-depleted zone created as a result of oxidation does not deviate substantially from the composition of the base material. These observations remain true whether one examines the isothermally treated specimen at 900 °C for 100 hours (Figure 13) or considers the case of the continuous ORD on the turbine blade removed from service (Figure 11(a)). By contrast, the composition of the alloy-depleted zone created at 1000 °C (Figure 13) lies clearly in the single-phase γ field, a substantial deviation from the base metal composition after only 100 hours of exposure. Further insight is gained into the difference between the oxidation characteristics at 900 °C and those at 1000 °C, through examining the time dependence of the composition of the advancing ORD front, as shown in Figure 14. The composition at the tip of the advancing ORD front, as measured through EDX analysis, is expressed as Σ Ni/(Σ Ni + Σ Al) on the binary Ni/Al phase diagram of the figure. It is seen from Figure 14 that an isothermal exposure of 20 hours creates the β phase at 900 °C as well as at 1000 °C. However, differences are seen at longer exposures. At 900 °C, increasing the exposure time to 40 and 100 hours does not change the composition at the tip of the ORD, although the ORD grows as a result of longer exposures. An implication is that, at 900 °C, the β phase continues to form as a result of oxidation as time goes on. Moreover, since the formation of the β phase is the precursor to internal oxidation in this alloy, as oxygen penetrates deeper into the material, the FSZ would continue to grow as a result. This is, in fact, observed on the turbine blade, with the formation of an ORD over 200 μm thick and an associated NiO external scale 135 μm thick (Figure 3(a)). Similarly, in the isothermal test conducted at 900 °C (Figure 8), the mass gain continues, with time indicating continued oxidation.

In contrast to the continued mass gain with time at 900 °C, there appears to be a vast reduction in the rate of oxidation at 1000 °C, following an initial period of rapid mass gain (Figure 8). Figures 13 and 14 provide insight into the process responsible for these characteristic features observed at 1000 °C. Although the composition of the advancing tip of the ORD does not change with time after an initial exposure of 20 hours at 900 °C, it does continue to change with time beyond 20 hours, upon isothermal exposure to 1000 °C (Figure 14). The nature of this change is such that, at times in excess of 40 hours at 1000 °C, the δ phase (Ni_2Al_3 on the binary system) begins to form at the tip of the advancing ORD. As seen from Figure 13, the tendency to form the δ phase is also indicated from the composition *vs* depth profiles generated on the transverse section of the disc isothermally treated for 100 hours at 1000 °C. Although the XRD and the EDX data obtained in the present work suggest that the δ phase is formed as a result of the oxidation of CMSX-10 at 1000 °C, it is felt that there remains a need for better corroboration, possibly through future work involving transmission electron microscopy (TEM).

It would appear that the formation of the δ phase in place of β slows down further oxidation at 1000 °C. As seen from Figure 13, the ORD resulting from a treatment for 100 hours at 900 °C has penetrated deeper into the material than that from a treatment of the same duration at 1000 °C. However, before considering the reasons for the effectiveness of the δ phase in slowing down the oxidation of CMSX-10 at 1000 °C, it is noteworthy that the formation of the β phase containing 50 at. pct Ni would also reduce the rate of oxidation, since

this intermetallic compound has the lowest diffusion coefficient at stoichiometry, and deviation from stoichiometry, be it on the Ni-rich side or the Al-rich side, increases the diffusion coefficient.[36]

Since the present work indicates that the formation of the δ phase may be responsible for the vastly reduced rate of oxidation following the early rapid oxidation at 1000 °C (Figures 8, 13, and 14), one should compare the diffusion coefficient of the δ phase in relation to that of the β phase. Diffusion coefficients have been measured earlier for the binary δ phase at temperatures below 655 °C,[40,41] and between 870 °C to 1000 °C.[42,43] Fortunately, Hickle and Heckel have made measurements of the diffusion coefficients in the β and the δ phases simultaneously, using the growth kinetics of these two phases formed as a result of the diffusion coating of nickel.[42] It was found that, at 1000 °C, diffusion occurs faster (by 3 times) in the β phase than it does in the δ phase, even though the reverse is true at lower temperatures.

The δ phase exists as an intermetallic compound over a composition range, as does the β phase, although the composition range of δ is narrower, since it is approximately 37 to 41 at. pct Ni. It is conceivable that the stoichiometric composition (Ni_2Al_3) has a minimum diffusion coefficient, as is the case with the β phase noted earlier. However, a systematic measurement of the variation of the diffusion coefficient with composition is currently lacking. Should the δ phase be responsible for the vastly reduced oxidation rate following the initial rapid oxidation of CMSX-10 at 1000 °C (Figure 8), and should there also be a minimum at its stoichiometric composition, it will have interesting consequences for the oxidation of CMSX-10 at temperatures above 1000 °C. From the binary phase diagram (Figure 14), it is seen that the range of composition over which the δ phase remains stable narrows with increasing temperature, attaining the stoichiometric composition at 1133 °C. Hence, at that elevated temperature, the δ phase formed would be most effective in slowing down oxidation. The implication is that the oxidation rate should decrease with increasing temperature above 1000 °C, attaining a minimum at around 1133 °C. Moreover, above 1133 °C, the rate of oxidation would be expected to rise again, because the δ phase is not stable at those elevated temperatures. Experiments are currently underway to test this hypothesis.

Finally, it may be noted that, although Al_2O_3 and the spinel $Ni(Cr,Al)_2O_4$ are not formed upon oxidation of CMSX-10 at temperatures below 1000 °C, a hard and therefore abrasion-resistant FSZ is formed (Figure 10). Moreover, the hardness of the FSZ increases with an increase in the temperature at which oxidation takes place. Furthermore, there is indication from the present work that the formation of the δ phase at 1000 °C creates a barrier to diffusion, thereby vastly reducing the rate of further oxidation. Hence, there exists the possibility of preoxiding at a higher temperature a component such as a turbine blade made of CMSX-10, prior to it being placed in service for operation at a lower temperature. For example, a prior oxidation for 50 hours at 1000 °C may impart an abrasion-resistant coating and a diffusion barrier adequate for the blade to operate at 900 °C in service without the need for aluminization. Although the viability of this concept remains to be tested on CMSX-10 through further experimentation, it is of note that the preservice oxidation of gas turbine discs and seals has been proposed recently as a means of preventing oxidation and corrosion of the superalloys in service.[44]

V. SUMMARY AND CONCLUSIONS

The following conclusions have been drawn from this work.

1. The formation of the external (Ni,Co)O scale initiates the process of oxidation. However, a discontinuous reaction requiring nucleation and growth leads to the formation of the internal oxidation zone.
2. The intermetallic β phase forms as a result of Ni (and Co) depletion from the ($\gamma + \gamma'$) matrix of the superalloy as the precursor to internal oxidation. The formation of the β phase resulting from oxidation, termed self-aluminization, does not appear to have been observed earlier in the superalloys.
3. Alumina (Al_2O_3) and the spinel $Ni(Cr,Al)_2O_4$, which are commonly observed in the internal oxidation zone of the first- and second-generation Ni-base superalloys, are not formed as a result of the oxidation of the third-generation alloy CMSX-10 at temperatures up to 1000 °C. Instead, the internal oxidation of the CMSX-10 leads to the formation of $(Ni,Co)Ta_2O_6$, $(Ni,Co)WO_4$, $CrTaO_4$, and $Cr(W,Mo)O_4$.
4. The formation of $(Ni,Co)Ta_2O_6$ and other oxides imparts a high hardness to the FSZ, thus offering the possibility that the internal oxidation zone of this alloy may be abrasion resistant.
5. There is indication that the formation of the δ phase (Ni_2Al_3) vastly reduces the oxidation rate after the initial rapid oxidation at 1000 °C.
6. Isothermal tests conducted in the laboratory at 900 °C produced a microstructure as well as profiles of composition and microhardness that were similar to those observed on the blade removed from service.

ACKNOWLEDGMENTS

The authors acknowledge the support of the Natural Sciences and Engineering Research Council of Canada, the Canadian Fund for Innovation, and the Canada Research Chair. One of the authors (MH) acknowledges the award of an EPSRC studentship at the University of Cambridge, and additional funding from Rolls-Royce plc. Contributions were made by Mr. Darren Mayne in specimen preparation and by Ms. Mary Mager in assisting with the SEM. Those contributions are also gratefully acknowledged.

REFERENCES

1. M. Göbel, A. Rahmel, and M. Schütze: *Oxid. Met*., 1993, vol. 39, pp. 231-61.
2. M. Göbel, A. Rahmel, and M. Schütze: *Oxid. Met*., 1994, vol. 41, pp. 271-300.
3. R. Janakiraman, G.H. Meier, and F.S. Pettit: *Metall. Mater. Trans. A*, 1999, vol. 30A, pp. 2905-13.
4. V.K. Tolpygo, D.R. Clarke, and K.S. Murphy: *Metall. Mater. Trans. A*, 2001, vol. 32A, pp. 1467-78.
5. J. Angenete, K. Stiller, and V. Langer: *Oxid. Met*., 2003, vol. 60. pp. 47-82.
6. J. Angenete and K. Stiller: *Oxid. Met*., 2003, vol. 60, pp. 83-101.
7. M.S. Hook: Ph.D. Thesis, University of Cambridge, Cambridge, United Kingdom, 2004.
8. U. Krupp and H.J. Christ: *Metall. Mater. Trans. A*, 2000, vol. 31A, pp. 47-56.
9. M.C. Maris-Sida, G.H. Meier, and F.S. Petit: *Metall. Mater. Trans. A*, 2003, vol. 34A, pp. 2609-19.

10. M.H. Li, X.F. Sun, T. Jin, H.R. Guan, and Z.Q. Hu: *Oxid. Met*., 2003, vol. 59, pp. 591-605.
11. M.H. Li, X.F. Sun, T. Jin, H.R. Guan, and Z.Q. Hu: *Oxid. Met*., 2003, vol. 60, pp. 195-210.
12. F.H. Yuan, E.H. Han, C.Y. Jo, T.F. Li, and Z.Q. Hu: *Oxid. Met*., 2003, vol. 60, pp. 211-24.
13. G.E. Fuchs: *Mater. Sci. Eng. A*, 2001, vol. 300, pp. 52-60.
14. M.A. Smith, W.E. Frazier, and B.A. Pregger: *Mater. Sci. Eng*., 1995, vol. A203, pp. 388-98.
15. M. Moniruzzaman, M. Maeda, Y. Murata, and M. Morinaga: *Iron Steel Inst. Jpn. Int*., 2003, vol. 43, pp. 386-93.
16. S. Ochiai, Y. Oya, and T. Suzuki: *Bull. P.M.E. (Tokyo Inst. Technol.)*, 1983, vol. 52, pp. 1-17.
17. S. Ochaiz, Y. Mishima, and T. Suzuki: *Bull. P.M.E. (Tokyo Inst. Technol.)*, 1984, vol. 53, pp. 15-28.
18. Pierre Caron: ONERA, CHATI-LON CEDEX, France, 2003 personal communication.
19. C.S. Giggins and F.S. Pettit: *J. Electrochem. Soc*., 1971, vol. 118, pp. 1782-90.
20. A. Ul-Hamid: *Oxid. Met*., 2002, vol. 58, pp. 41-56.
21. D.K. Das, V. Singh, and S.V. Joshi: *Mater. Sci. Technol*., 2003, vol. 19, pp. 695-708.
22. M.J. Stiger, N.M. Yanar, M.G. Topping, F.S. Pettit, and G.H. Meier: *Z. Metallkd*., 1999, vol. 90, pp. 1069-78.
23. E.A.G. Shillington and D.R. Clarke: *Acta Mater*., 1999, vol. 47, pp. 1297-1305.
24. P. Nash, M.F. Singleton, and J.I. Murray: in *Phase Diagrams of Binary Nickel Alloys*, P. Nash, ed., ASM INTERNATIONAL, Materials Park, OH, 1991, p. 3.
25. O. Kubaschewski and B.E. Hopkins: *Oxidation of Metals and Alloys*, 2nd ed., Butterworths, London, 1962, pp. 8-33.
26. B. Jönsson: *Scand. J. Metall*., 1995, vol. 24, pp. 21-27.
27. S.B. Jung, T. Yamane, Y. Minamino, K. Hirao, H. Araki, and S. Saji: *J. Mater. Sci. Lett*., 1992, vol. 11, pp. 1333-37.
28. R.A. Swalin and A. Martin: *Trans. AIME*, 1956, vol. 206, pp. 567-72.
29. N. Komai, M. Watanabe, Z. Horita, T. Sano, and M. Nemoto: *Acta Mater*., 1998, vol. 46, pp. 4443-51.
30. A. Davin, V. Leroy, D. Coutsouradis, and L. Habraken: *Cobalt*, 1963, vol. 19, pp. 51-56.
31. D. Bergner: *Krist. Technol*., 1972, vol. 7, p. 651.
32. M.S.A. Karunaratne, P. Carter, and R.C. Reed: *Mater. Sci. Eng. A*, 2000, vol. 281, pp. 229-33.
33. K. Hoshino, S.J. Rothman, and K.S. Averback: *Acta Metall*., 1988, vol. 36, pp. 1271-79.
34. Y. Minamino, S.B. Jung, T. Yamane, and K. Hirao: *Metall. Trans. A*, 1992, vol. 23A, pp. 2783-90.
35. J. Cermac and V. Rothova: *Acta Mater*., 2003, vol. 51, pp. 4411-21.
36. S. Kim and Y.A. Chang: *Metall. Mater. Trans. A*, 2000, vol. 31A, pp. 1519-24.
37. O. Kubaschewski, E.L. Evans, and C.B. Alcock: *Metallurgical Thermochemistry*, Pergaman Press, Oxford, United Kindom, 1967, pp. 210-15.
38. W. Huang and Y.A. Chang: *Intermetallics*, 1998, vol. 6, pp. 487-98.
39. A.M. Venezia, J.E. Baker, and C.M. Loxton: *Proc. 7th Int. Conf. SIMS 7*, 1990, pp. 719-22.
40. L.S. Castleman and L.L. Seigle: *Trans. TMS-AIME*, 1958, vol. 212, pp. 589-96.
41. M.M.P. Janssen and A.D. Rieck: *Trans. TMS-AIME*, 1967, vol. 239, pp. 1372-85.
42. A.J. Hickl and R.W. Heckel: *Metall. Trans. A*, 1975, vol. 6A, pp. 431-40.
43. A.K. Sarkhel and L.L. Seigle: *Metall. Trans. A*, 1982, vol. 13A, pp. 1313-14.
44. M.J. Weimer, B.A. Nagraj, J.C. Schaeffer, and J.A. Heaney III: European Patent 1,295,960 A2, March 26, 2003.